





Active laminated-plate model for spontaneous bending of *Hydra* tissue fragments driven by supracellular actomyosin bundles

Jian Su ^{1,2,3}, Haiqin Wang ^{1,2,3}, Zhongyu Yan ^{1,2} & Xinpeng Xu ^{1,2}✉

The outstanding regeneration of *Hydra*'s excised tissue fragments occurs via initial spontaneous bending to some quasi-stable shape in several minutes. However, the underlying mechanism and dynamics of such initial spontaneous bending are still debated. Here, we propose that the spontaneous bending is driven mechanically by supracellular actomyosin bundles inherited from parent *Hydra*. Our active laminated-plate (ALP) model predicts that the equilibrium fragment shape is determined by anisotropy in contractility and elasticity. We construct a minimal dynamic ALP model including three dissipation mechanisms. By variational analysis and bead-spring simulations, we find that the bending process starts diffusively from the edges and relaxes exponentially to the equilibrium shape. The different dissipation mechanisms take place at distinct timescales: the viscous drag occurs in 0.001 seconds, while the interlayer frictional sliding and cellular dissipation take place in minutes. The ALP model could be adapted to study multi-layered viscoelastic tissues with nematic cytoskeletal structures and provides a useful framework for tissue morphogenesis and regeneration.

¹Technion - Israel Institute of Technology, Haifa 3200003, Israel. ²Department of Physics and MATEC Key Lab, Guangdong Technion - Israel Institute of Technology, 241 Daxue Road, Shantou 515063 Guangdong, China. ³These authors contributed equally: Jian Su, Haiqin Wang. ✉email: xu.xinpeng@gtit.edu.cn

Hydra is a multicellular fresh-water polyp, which exhibits remarkable regeneration capabilities, making it an excellent model system for studying tissue morphogenesis^{1–6}. The *Hydra* body consists of a single-axis hollow-cylindrical tube (about 5–10 mm long)¹, which has a triple-layer structure composed of two epithelial cell layers (endoderm and ectoderm) that are adhered together by an intermediate soft layer of extracellular matrix (called mesoglea) as shown in Fig. 1a. *Hydra* body shape is maintained by a contractile actomyosin cytoskeleton^{4–7}, which shows a highly-aligned orientation over supracellular scales (see Fig. 1a): the actomyosin bundles takes longitudinal orientation (along the tube axis) in the ectoderm and circumferential orientation in the endoderm. Regenerating *Hydras* use their cytoskeleton to regulate their cells and to guide the regeneration process^{4–7}. When fragments are excised from the adult *Hydra* body, the supracellular pattern of cytoskeletal bundles is inherited, survives, and finally becomes a part of the new daughter *Hydra*. These supracellular cytoskeletal bundles provide structural “memory” of the alignment along the body axis^{4–7}. They generate mechanical forces and direct the alignment of the cytoskeleton in regions where the supracellular order is lacking in the early stage of regeneration.

At the initial stage of the regeneration of *Hydra* tissue fragments that are excised freshly from adult *Hydra* body^{7,8}, the fragments bend spontaneously to some quasi-stable (or mechanical-equilibrium) shape in several minutes (see Fig. 1b). Subsequently, the cytoskeleton of the fragment remodels to find a balance between maintaining its pre-existing organization and adapting to the new curved conditions^{4–7}. After about one hour of the bending-remodeling loop, the excised fragments fold into small hollow spheroids^{4–8}.

In this work, we focus on the modeling and analysis of the initial spontaneous bending of *Hydra* fragments that happens in the first several minutes after their excision from parent *Hydra* (see Fig. 1a, b). We propose that such spontaneous tissue bending is an active process driven mechanically by the contractions of the two sets of aligned, supracellular actomyosin bundles. We assume that the short bending process is accompanied by changes only in cell shape and structure, but not in cell division and apoptosis⁹. The equilibrium bent shape of *Hydra* tissue fragments is then determined by the balance between the actomyosin contractile forces and the elastic restoring forces due to cell-shape deformation⁹. The bending dynamics are driven by the active and elastic forces that are balanced by some dissipative forces. In the context of *Hydra* tissue, we identify three types of dissipation mechanisms: (i) the fragment motion relative to surrounding viscous fluids, (ii) the relative frictional slide between adjacent tissue layers¹⁰, and (iii) the cellular dissipation associated with sub-cellular-scale remodeling and cellular-scale rearrangements^{9,11,12}.

Based on the above assumptions, we construct an active laminated-plate (ALP) model that connects the triple-layer structure and the contractile supracellular actomyosin bundles of *Hydra* fragments with the equilibrium shape and dynamics of their spontaneous bending (see Fig. 1a). We predict that the bent shape of plate-like *Hydra* fragments characterized by their spontaneous curvature tensor is mostly determined by their anisotropy in both the supracellular actomyosin contractility and the elastic properties of each lamina layer, as summarized in Fig. 2a, b. For the bending dynamics of rod-like tissue fragments, we present a minimal model based on the static ALP model and carry out analysis using an approximate variational method (based on Onsager’s variational principle^{13,14}) and bead-spring simulations. We find that the tissue bending propagates diffusively from the edges into the center (with the bent length being proportional to the square root of time). Whereas, when the bending is close to its final equilibrium shape, the end-to-end (ETE) distance decays exponentially with time toward its equilibrium value. Moreover, we suggest that the interlayer frictional sliding and cellular dissipation set the dominant timescale (of minutes) observed in experiments during the initial spontaneous bending of *Hydra* fragments^{4–7}.

Results

Spontaneous curvature of *Hydra* tissue fragments driven by uniform supracellular contraction. To construct a continuum model for *Hydra* tissue fragments, we first note a structural analogy between *Hydra* fragments (with triple-layer structure) and composite laminated plates in material science^{15,16}. Moreover, we find that in typical regeneration experiments^{4–7}, the lateral lengths of *Hydra* fragments are usually $\sim 100\ \mu\text{m}$ much larger than their thickness $h \sim 10\ \mu\text{m}$. We then formulate an active (thin) laminated-plate (ALP) model¹⁷ (see Sec. A of Supplementary Note 1) for *Hydra* fragments by following the classical (thin) laminated-plate theory¹⁶ that extends the classical (thin) plate (CP) theory¹⁵ of mono-layer isotropic materials to multi-layer orthotropic materials. In our ALP model, the *Hydra* fragment is modeled as a triple-layer laminated plate (see Fig. 1a). The equilibrium bent shape of a *Hydra* fragment at small deformation is characterized by spontaneous curvature tensor and determined by minimizing the deformation energy of the laminate fragment upon internal uniform active contractions applied by two sets of perpendicular supracellular actomyosin bundles. Note that, mathematically, such an ALP model is very similar to the model for elastic lamellae with assorted pre-stresses that are set by deformation of “active” thermo- or photo-sensitive elements in composite materials¹⁸, non-uniform in-plane growth¹⁹, or absorbing/expelling water²⁰ in plant sheets, etc.

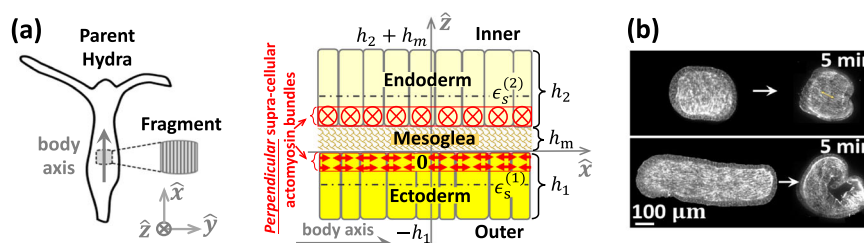


Fig. 1 Schematic illustration of the triple-layer structure of *Hydra* fragments and experimental observation of the initial spontaneous bending.

a Schematic illustration of the *Hydra* body plan and the triple-layer structure of *Hydra* fragments: ectoderm cell layer (yellow), endoderm cell layer (light yellow), and intermediate soft matrix (mesoglea). Two sets of perpendicular supracellular actomyosin bundles (red arrows) are formed on the basal sides of each epithelial layer. Interlayer slides are characterized by the misfit strains $\epsilon_s^{(1)}$ and $\epsilon_s^{(2)}$ of the two cell layers relative to the mesoglea layer, respectively. **b** Experimental observations: spontaneous bending of freshly excised *Hydra* (plate- and rod-like) tissue fragments to quasi-stable (equilibrium) bent shape in several minutes. Reproduced from ref. 7 with permission from Elsevier.

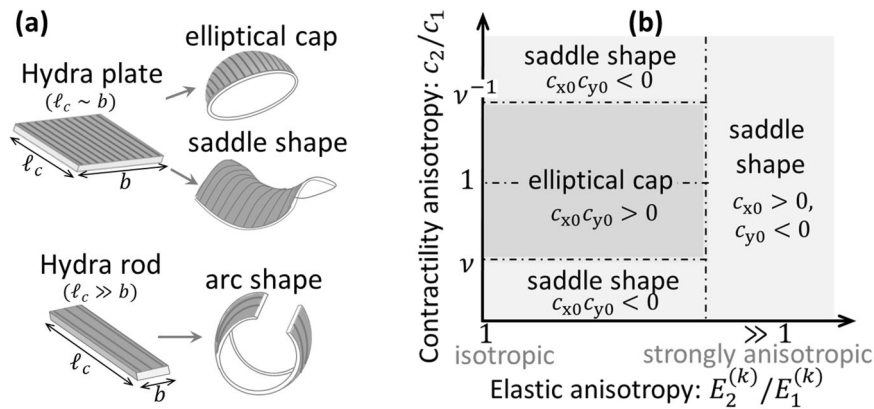


Fig. 2 Schematic illustration of the spontaneous bent shape of *Hydra* fragments driven by uniformly contracting supracellular actomyosin bundles. **a** Schematic illustration for the spontaneous bent shape of *Hydra* fragments driven by uniformly contracting supracellular actomyosin bundles. The contour length, width, and total thickness of the fragments are denoted by ℓ_c , b , and h , respectively. **b** A schematic bent-shape diagram of *Hydra* plates with different anisotropy in actomyosin contractility (measured by c_2/c_1) and in elasticity (measured by $E_2^{(k)}/E_1^{(k)}$ in each $k = 1, m, 2$ lamina layer). Here c_i characterizes the contractility of the two sets of perpendicular supracellular bundles; $E_1^{(k)}$ and $E_2^{(k)}$ are the two principal Young's moduli of each ($k = 1, m, 2$) orthotropic lamina layer.

Firstly, for *Hydra* fragments consisting of isotropic lamina layers, the total bending energy density (per area) is found to be¹⁷ (see Sec. A of Supplementary Note 1)

$$F_b = \frac{1}{2} D_p (c_x^2 + 2\nu c_x c_y + c_y^2) - (M_p^{(1)} c_x + M_p^{(2)} c_y). \quad (1)$$

Here D_p is the effective flexural stiffness. The Poisson ratio ν is assumed to be constant. c_x and c_y are the two principal curvatures of the neutral surface located at $z = z_0$. $M_p^{(1)} \approx \tau_p^{(1)} z_0$, $M_p^{(2)} \approx \tau_p^{(2)} (z_0 - h_m)$, and $\tau_p^{(1)}, \tau_p^{(2)} < 0$ are the active torques and contractile forces generated by the two sets of supracellular actomyosin bundles, respectively. The position of the neutral surface is given by (see Sec. B of Supplementary Note 1)

$$z_0 = \frac{E_*^{(2)} [(h_2 + h_m)^2 - h_m^2] + E_*^{(m)} h_m^2 - E_*^{(1)} h_1^2}{2[E_*^{(1)} h_1 + E_*^{(m)} h_m + E_*^{(2)} h_2]}. \quad (2)$$

with $E_*^{(k)} \equiv E^{(k)}/(1 - \nu^2)$; $E^{(k)}$ and h_k ($k = 1, m, 2$) being Young's modulus and thickness of the ectoderm, mesoglea, and endoderm, respectively. Note that in comparison to the bending energy with a quadratic form of principal curvatures in CP theory¹⁵, terms coupling active actomyosin torques linearly with curvatures^{21,22} also appear in Eq. (1), resulting in non-zero spontaneous curvatures.

Minimizing $\mathcal{F}_b = \int dx dy F_b$ gives the spontaneous curvatures:

$$c_{x0} = \frac{c_1 - \nu c_2}{1 - \nu^2}, \quad c_{y0} = \frac{c_2 - \nu c_1}{1 - \nu^2}, \quad (3)$$

with $c_i = M_p^{(i)}/D_p$ ($i = 1, 2$) characterizing the contractility of the two sets of supracellular actomyosin bundles, respectively. From Eq. (3), we see that the spontaneous bending (with non-zero c_{x0} and/or c_{y0}) of *Hydra* fragments is driven by the supracellular actomyosin contraction (represented by non-zero $\tau_p^{(i)}$) that occurs away from the neutral surface at $z = z_0$. Moreover, we find from Eq. (3) that the principal curvatures (and the equilibrium bent shape) are mainly determined by the contractility anisotropy measured by c_2/c_1 . If $\nu < c_2/c_1 < \nu^{-1}$, the *Hydra* fragments will bend spontaneously to an elliptical cap shape; otherwise, they will bend to a saddle shape as summarized in Fig. 2b.

Secondly, for tissue fragments consisting of strongly anisotropic lamina layers (for example, due to the presence of aligned thick actomyosin bundles in the two epithelial layers), we find that the spontaneous bending in the two principal directions is almost independent (see Sec. A of Supplementary Note 1), and the neutral surfaces of the spontaneous bending lie in different

layers for bending along different directions: in ectoderm for bending along the \hat{x} -direction and in endoderm for bending along the \hat{y} -direction, respectively. In this case, the two principal spontaneous curvatures are given by $c_{x0} \approx c_1 > 0$, $c_{y0} \approx c_2 < 0$, that is, the fragments bend spontaneously to be saddle shape (see Fig. 2b).

Next, based on the above results, we can connect the triple-layer structure and elastic/geometric properties of *Hydra* fragments with their equilibrium bent shapes observed in experiments⁷ (see Fig. 1b). *Hydra* fragments bend spontaneously to a spherical cap shape toward the inner endoderm side, that is, $c_{x0} \approx c_{y0} > 0$, from which we draw the following conclusions. (i) The cap-like shape corresponds to the case of more-or-less isotropy in both contractility (of the two contractile bundles) and elasticity (of each lamina layer), as shown in Fig. 2b. (ii) The inward bending corresponds to $c_1, c_2 > 0$ (using Eq. (3)) and the case where the neutral surface lies in the ectoderm layer, i.e., $z_0 < 0$, as obtained using $c_1 \approx \tau_p^{(1)} z_0 / D_p > 0$ and $c_2 \approx \tau_p^{(2)} (z_0 - h_m) / D_p > 0$. Furthermore, from $z_0 < 0$ and Eq. (2), we obtain that the inward cap-bending needs to satisfy an inequality $E_{p,\text{eff}}^{(2)} (h_2 + h_m)^2 < E_*^{(1)} h_1^2$ with $E_{p,\text{eff}}^{(2)} \equiv E_*^{(2)} - (E_*^{(2)} - E_*^{(m)}) h_m^2 / (h_2 + h_m)^2$. Therefore, at given geometries (given thicknesses, h_k), the presence of a soft mesoglea layer with $E_*^{(m)} < E_*^{(2)}$ makes the inequality and $z_0 < 0$ easier to satisfy, thus facilitating inward tissue bending toward the endoderm side. Such a mesoglea-softening mechanism is similar to that of connecting a stiff spring to a soft spring in series. However, when $E_*^{(1)} h_1^2 < E_*^{(2)} [(h_2 + h_m)^2 - h_m^2]$, such a mesoglea-softening mechanism is impossible to ensure inward bending.

Before closing this section, we would like to present a simple way of finding the bending direction driven by each set of supracellular actomyosin bundles in a laminated tissue: comparing the position of contracting bundles to the location of the neutral surface, z_0 , given in Eq. (2). For example, in *Hydra* fragments (see Fig. 1a), the actomyosin bundle at the basal side of the ectoderm layer near $z = 0$ drives the bending toward the endoderm side if $z_0 < 0$, and toward the ectoderm side if $z_0 > 0$. Similarly, the actomyosin bundle at the basal side of the endoderm layer near $z = h_m$ drives the bending toward the endoderm side if $z_0 < h_m$, and toward the ectoderm side if $z_0 > h_m$. Therefore, in the *Hydra* tissue, an inward bending (toward the endoderm side) to an elliptical or spherical cap shape requires $z_0 < 0$, a condition that has already been obtained previously from $c_1, c_2 > 0$ and Eq. (3).

Spontaneous bending and interlayer slide of rod-like *Hydra* fragments. If instead of a *Hydra* plate, one cuts a rod-like *Hydra* fragment, the total bending energy density (per length) in Eq. (1) reduces to (see Sec. B of Supplementary Note 1):

$$F_b = \frac{1}{2} D_r c^2 - M_r c. \quad (4)$$

Here D_r is the effective flexural stiffness. c is the curvature of the neutral line at $z = z_0$. $M_r \approx \tau_r z_0$ and $\tau_r < 0$ are the active torque and contractile force generated by the actomyosin bundle in the ectoderm layer, respectively. The neutral line position z_0 is given by the same form as Eq. (2) but $E_*^{(k)}$ should be replaced by $E^{(k)b}$ with b being the width of the *Hydra* rod.

Minimization of $\mathcal{F}_b = \int dx F_b$ gives the spontaneous curvature (see Sec. B of Supplementary Note 1): $c_0 = M_r/D_r \approx \tau_r z_0/D_r$. Then using $D_r \sim E h^3 b$, $z_0 \sim h$, and noting that in typical cell experiments⁹: $\tau_r/hb \sim 0.1$ kPa, $h \sim 10$ μm , $E \sim 1$ kPa, we estimate the spontaneous curvature $c_0 \sim 1/100$ μm^{-1} . Interestingly, for *Hydra* regenerating from cell aggregates³, the curvature c_{s0} of the hollow *Hydra* spheroids formed from an aggregate of a minimal number of $N_c \sim 1000$ cells^{2,3} can be estimated to be the same scale $c_{s0} \sim 1/100$ μm^{-1} by calculating the surface area of the spheroid, $4\pi c_{s0}^{-2} \sim N_c R_c^2$, and using the cell size $R_c \sim 10$ μm . Moreover, such cell-scale curvature is also known to appear very often in many natural in vivo microenvironment²¹, e.g., cylindrical-shaped glands and blood vessels²³.

Note that the supracellular contraction and the elastic/geometric properties are generally non-uniform, hence the spontaneous curvature c_0 can be different at different positions through the fragments. In this case, for a freely suspending *Hydra* fragment, the equilibrium bent shape corresponds to the equilibrium state with bending energy minimized locally, that is, the local curvature equal to local c_0 . In contrast, the bent shape of a constrained *Hydra* rod is more complex. Some non-trivial periodic bent shapes have been obtained, as shown in Fig. S2 of Supplementary Note 1. The mechanistic perspective of the spontaneous bending of tissue fragments during morphogenesis conveyed in this work has been proposed before^{8,24–26}, and several classical theories have been developed. Among the earliest theories of this kind, W.H. Lewis proposed (1947)²⁴ a mechanical model of epithelial sheets, consisting of brass bars, tubes, and rubber bands (see Fig. S2 in Sec. C of Supplementary Note 1) for a schematic figure of the model). We discuss this model in Sec. C of Supplementary Note 1 and show the equivalence (the mapping) between Lewis' model and our ALP model in predicting the spontaneous bending shape of *Hydra* tissue.

In addition, during the tissue bending, the interlayer slide may occur between each cell layer and the intermediate mesoglea matrix¹⁰, as shown in Fig. 1a, and the fragment becomes incoherent²⁷. In this case, we neglect the in-plane contraction, and the total energy \mathcal{F}_t takes the following phenomenological form^{22,27}

$$\mathcal{F}_t = \int_{-\ell_c/2}^{\ell_c/2} ds \left[\frac{Y_s}{2} \epsilon_s^2 - \chi \epsilon_s c + \frac{D_r}{2} (c - \tilde{c}_0)^2 \right]. \quad (5)$$

Here ℓ_c is the rod contour length, \tilde{c}_0 being the spontaneous curvature of coherent fragments. ϵ_s denotes the interlayer slide or the misfit strain discontinuity at the cell-mesoglea interfaces, Y_s is the stiffness for the interlayer slide, and in the thin rod limit, the misfit interlayer displacement is simply given by $\epsilon_s h/2$ with h being the rod thickness. χ is the linear coupling coefficient between bending and interfacial slide. Note that in a complete triple-layer model (as shown in Fig. 1a and discussed in Sec. D of Supplementary Note 1 for the bending of *Hydra* tissue, we should introduce two slide strains or displacements at the two interfaces:

ectoderm-mesoglea interface and endoderm-mesoglea interface, respectively. However, for simplicity, we assume in a coarse-grained manner that one strain ϵ_s is enough to characterize the interlayer slide. The equilibrium bent state of the rod is then characterized by the spontaneous curvature $c_0 \equiv \tilde{c}_0 D_r / \tilde{D}_r$ and the equilibrium slide $\epsilon_{s0} = \chi c_0 / Y_s$ with $\tilde{D}_r \equiv D_r - \chi^2 / Y_s$ being the normalized flexural stiffness of the rod. Particularly, in the limit of $Y_s \rightarrow \infty$, we recover the case of coherent fragments with $c_0 = \tilde{c}_0$ and $\epsilon_{s0} = 0$ where the strain is continuous through the thickness.

Bending dynamics of *Hydra* tissue rods: effects of different dissipation mechanisms. We now consider the dynamic process of the spontaneous bending of *Hydra* tissue rods in surrounding viscous fluids starting from the initial state to the final equilibrium shape as shown in experiments (see Fig. 1b). The initial state of the *Hydra* fragment is assumed to be flattened to mimic the state when it is excised from the parent *Hydra*. The bending dynamics of long soft rods with non-zero spontaneous curvature c_0 and contour length $\ell_c \gg 2\pi R_0$ (with $R_0 = c_0^{-1}$) have been explored intensively in both theory and experiments^{28,29}. However, in typical *Hydra* regeneration experiments⁷, *Hydra* rods are usually short with $\ell_c \sim 2\pi R_0$. In this case, the total energy \mathcal{F}_t of the laminated *Hydra* rod is given by Eq. (5), and the bending dynamics is driven by the relaxation of stored elastic energy at the initial flattened state. Furthermore, the three types of dissipation mechanisms (arising from viscous drag by the surrounding fluids, the interlayer frictional sliding, and cellular remodeling/rearrangement inside the fragments) during the bending are taken into account by the dissipation function (see Sec. A of Supplementary Note 2)

$$\Phi = \int_{-\ell_c/2}^{\ell_c/2} ds \left[\frac{1}{2} \xi_v \dot{\mathbf{r}}^2 + \frac{1}{2} \xi_s \dot{\epsilon}_s^2 + \frac{1}{2} \eta_{\text{cell}} b h (\dot{h} c)^2 \right]. \quad (6)$$

Here $\mathbf{r}(s)$ is the position vector of points (parameterized by arc length s) on the rod, the local curvature c is given by its second derivatives³⁰, and the upper dot hereafter denotes the time derivative. ξ_v and ξ_s are the viscous drag coefficient per rod length and friction coefficient for interlayer sliding, respectively. Interestingly, interlayer frictional sliding has recently been found to be able to facilitate long-range force propagation in tissues that usually have multi-layer structures¹⁰. η_{cell} is an effective viscosity characterizing the additional cellular dissipation at sub-cellular and cellular scales.

We then use Onsager's variational principle^{13,14} and minimize Rayleighian $\mathcal{R}[\dot{\mathbf{r}}, \dot{\epsilon}_s] = \dot{\mathcal{F}}_t + \Phi$, yielding a set of highly nonlinear partial differential equation (e.g., Kirchhoff equations)²⁹. However, here we will not solve these nonlinear equations but carry out direct-variational analysis^{13,14} for the very initial bending stage near the flattened state and the final bending stage close to the equilibrium bent shape (see Sec. B of Supplementary Note 2).

Initially, near the flattened state (see Fig. 3a), we neglect the effects of the interlayer slide as well as cellular dissipation, and take the simplest continuous trial profile of local curvature $c(s, t)$ (see Fig. 3b):

$$c = \begin{cases} 0, & 0 \leq s < \ell_c/2 - a, \\ c_0(s - \ell_c/2)/a + c_0, & \ell_c/2 - a \leq s \leq \ell_c/2, \end{cases} \quad (7)$$

in which case the bending dynamic process is characterized by only one time-dependent parameter: the bent length $a(t)$ of the rod. Substituting the trial profile into Eqs. (5) and (6), we obtain the Rayleighian \mathcal{R} and its minimization with respect to \dot{a} gives

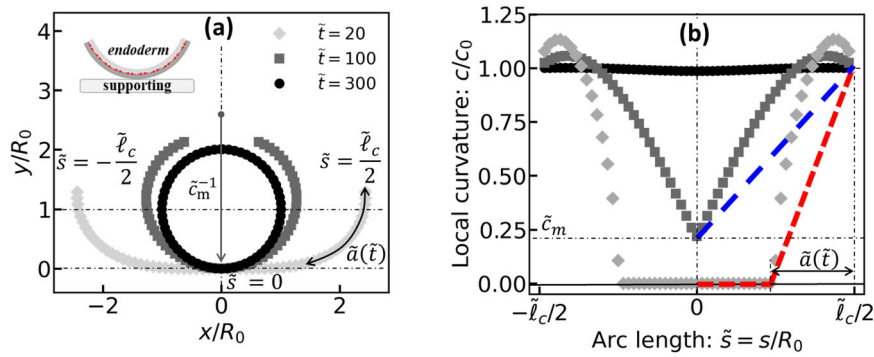


Fig. 3 Bead-spring simulations of the dynamic bending process of a *Hydra* rod. Simulation snapshots of the dynamic bending process of a *Hydra* rod (of contour length $\ell_c = 2\pi R_0$) in viscous fluids on a supporting surface: **a** the rod shape and **b** the curvature profile. In **b**, the linear trial profiles of curvature for variational analysis are plotted (dashed lines), which are parameterized by the bent length $\tilde{a} = a/R_0$ for the initial stage (red dashed line) and the center curvature $\tilde{c}_m = c_m/c_0$ for the final stage (blue dashed line), respectively.

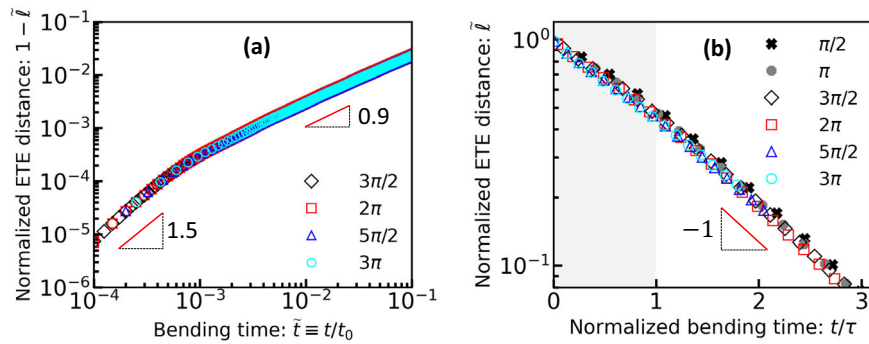


Fig. 4 Temporal evolution of the end-to-end (ETE) distance $\tilde{\ell}$ for *Hydra* rods. **a** The initial bending starting diffusively from the edges and **b** the final bending relaxing exponentially to the equilibrium shape. Universal scaling relations are found for rods of different contour lengths $\pi/2 \leq \tilde{\ell}_c \leq 3\pi$.

(see Sec. B of Supplementary Note 2)

$$a \approx \left(\frac{2\tilde{D}_r c_0^2}{3\xi_v} \right)^{1/2} t^{1/2}, \quad (8)$$

that is, the bending starts from the edges and propagates diffusively into the center. Moreover, from Eq. (8) we calculate the normalized ETE distance $\tilde{\ell} \equiv (\ell - \ell_{\text{eq}})/(\ell_c - \ell_{\text{eq}})$ scaling as $1 - \tilde{\ell} \sim a^3 \sim t^{3/2}$, where ℓ is the ETE distance with ℓ_{eq} being its equilibrium value. Interestingly, although the linear trial curvature profile assumed in Eq. (7) has some visible deviation from the simulated profile (as shown in Fig. 3b), the scaling law predicted above for ETE distance agrees well with simulation results in Fig. 4a and is not sensitive to the form of trial curvature profile; the same scaling is obtained by using a simpler trial step-function profile of curvature. However, we note that the initial diffusive bending process happens only in a very short period, as shown in Fig. 4a. The bending dynamics slow down quickly from the diffusive regime to a subdiffusive regime with $1 - \tilde{\ell} \sim t^{0.9}$.

In the final stage of the bending dynamics close to the equilibrium bent state (see Fig. 3a), we take the same strategy as above and also choose a linear trial profile of the curvature $c(s, t)$ (see Fig. 3b) and the interlayer slide $\epsilon_s(s, t)$ as

$$\begin{aligned} c &= c_m + (2s/\ell_c)(c_0 - c_m), \\ \epsilon_s &= \epsilon_{s,m} + (2s/\ell_c)(\epsilon_{s0} - \epsilon_{s,m}), \end{aligned} \quad (9)$$

for $0 \leq s \leq \ell_c/2$, in which case the bending dynamic process is described by the two time-dependent parameters: the curvature $c_m(t)$ and interlayer slide $\epsilon_{s,m}(t)$ in the rod center at $s=0$. Substituting the trial profile into Eqs. (5) and (6), we obtain the Rayleighian \mathcal{R} and its minimization yields (see Sec. D of

Supplementary Note 2)

$$\begin{aligned} (\tau + \tau_{\text{cell}})\dot{\tilde{c}}_m &= 1 - (1 + \mathcal{B})\tilde{c}_m + \mathcal{B}\tilde{\epsilon}_{s,m}, \\ \tau_s \dot{\tilde{\epsilon}}_{s,m} &= \tilde{c}_m - \tilde{\epsilon}_{s,m}, \end{aligned} \quad (10)$$

with $\tilde{c}_m = c_m/c_0$ and $\tilde{\epsilon}_{s,m} = \epsilon_{s,m}/\epsilon_{s0}$. Here $\mathcal{B} = Y_s \epsilon_{s0}^2 / c_0^2 \tilde{D}_r$ characterizes the relative stiffness of interlayer slide and out-plane bending and it is order unity since all energy terms in Eq. (5) are comparable. The three characteristic timescales $\tau = 6\xi_v \mathcal{L} / \tilde{D}_r c_0^4$, $\tau_{\text{cell}} = \eta_{\text{cell}} b h^3 / \tilde{D}_r$, and $\tau_s = \xi_s / Y_s$ are associated with viscous drag, sub-cellular or cellular dissipation, and interlayer frictional sliding, respectively. \mathcal{L} is a nonlinear function of rod contour length ℓ_c (changing from 0 to order one; see its expression in Eq. (S79) of Supplementary Note 2).

We consider the following two limits of the dynamic equation (10) that are particularly interesting and may be relevant to the bending dynamics during tissue morphogenesis and regeneration. Firstly, in the limits of either coherent *Hydra* rods or incoherent *Hydra* rods with small friction, we have $\tau_s / (\tau + \tau_{\text{cell}}) \ll 1$, and the viscous drag from the surrounding fluids or the cellular dissipation is the dominant dissipation mechanism. In this limit, we find from Eq. (10) the normalized ETE distance $\tilde{\ell}(t)$ follows

$$\tilde{\ell} \sim \exp[-t/(\tau + \tau_{\text{cell}})], \quad (11)$$

which has been justified for rods with various contour lengths by our numerical simulations using the bead-spring model and shown in Fig. 4(b). Note that the relaxational time $\tau = 6\xi_v \mathcal{L} / \tilde{D}_r c_0^4$ shows a nonlinear dependence on the rod contour length ℓ_c (due to the nonlinear function \mathcal{L}): τ is small for short rods $\ell_c < \pi R_0$, but increases very fast with increasing ℓ_c when $\ell_c > \pi R_0$. For example, the time $\tau \sim \xi_v / \tilde{D}_r c_0^4$ for $\ell_c = 2\pi R_0$ is about ten times larger than

that for $\ell_c = \pi R_0$. In addition, we have used the bead-spring model to numerically examine the bending dynamics of *Hydra* rods under some different boundary conditions (see Figs. S5–S7 in Sec. C of Supplementary Note 2). We find that the bending dynamics predicted above are very robust: the same scaling laws (including the nonlinear contour-length dependence of relaxational time τ due to \mathcal{L}) are found for most different boundary conditions, including both the initial diffusive bending and the final relaxational bending processes.

Secondly, in the limit of incoherent *Hydra* rods with large friction, we have $\tau_s/(\tau + \tau_{\text{cell}}) \gg 1$, we obtain from Eq. (10) the ETE distance $\tilde{\ell}(t)$ following the same exponential form:

$$\tilde{\ell} \sim \exp(-t/\tau_s). \quad (12)$$

That is, in either limit, the characteristic time for the spontaneous bending of the tissue rod is controlled by the slowest dissipative dynamics and the longest timescale. Particularly for *Hydra* tissue rods, we can estimate the magnitude of the three timescales as follows. Using $\bar{D}_r \sim Eh^3b$, $\xi_v \sim \eta_{\text{env}}$, $b \sim 10h$, $Y_s \sim Ehb$, and $\xi_s = \xi h^2b$, we obtain $\tau \sim \eta_{\text{env}}/Eh^3bc_0^4$, $\tau_{\text{cell}} \sim \eta_{\text{cell}}/E$, and $\tau_s \sim \xi h/E$ with η_{env} being the viscosity of surrounding fluids and ξ being the interlayer friction coefficient¹⁰. We can then substitute typical parameter values and obtain

$$\tau \sim 10^{-3} \text{ s}, \quad \tau_{\text{cell}} \sim \tau_s \sim 1 \text{ min}, \quad (13)$$

where the parameter values are taken from cell experiments^{9,10}: $h \sim 10 \mu\text{m}$, $c_0 \sim 1/100 \mu\text{m}^{-1}$, $E \sim 1 \text{ kPa}$, $\eta_{\text{env}} \sim 10^{-3} \text{ Pa} \cdot \text{s}$, and $\xi \sim 10^{10} \text{ Pa} \cdot \text{s} \cdot \text{m}^{-1}$. Particularly, we have taken $\eta_{\text{cell}} \sim 10^5 \text{ Pa} \cdot \text{s}$, a magnitude measured in the study of mouth opening dynamics of *Hydra*⁹, and for spherical cellular aggregates¹¹ and zebrafish embryonic tissues³¹. Therefore, the spontaneous bending of *Hydra* rods is controlled by the dissipation due to interlayer frictional sliding and/or the sub-cellular/cellular dissipation that sets the longest characteristic timescales $\tau_{\text{cell}} \sim \tau_s \sim 1 \text{ min}$ consistent with the time duration of initial spontaneous bending observed in *Hydra* regeneration experiments (see Fig. 1b)⁷. In this case, with $\tau_{\text{cell}} \sim \tau_s \gg \tau$, the approximate bending dynamics is described by Eq. (10) with τ set to be zero.

Discussions

The active laminated-plate (ALP) model constructed here for *Hydra* tissue fragments connects the triple-layer tissue structure and the contractile supracellular actomyosin bundles of fragments with the equilibrium shape and dynamics of their spontaneous bending. In this model, the equilibrium bent shape of a *Hydra* fragment is characterized by spontaneous curvature tensor and determined by minimizing the deformation energy of the laminate fragment upon internal uniform active contractions applied by two sets of perpendicular supracellular actomyosin bundles. The concept of spontaneous curvature has been used a long time ago to represent the tendency of lipids to curve in lipid membranes³⁰ and to describe the spontaneous bending of uniformly-heated bimetal plates³², in which the driving forces are chemical heterogeneity and asymmetric thermal expansion, respectively. In contrast, the spontaneous bending of tissue fragments proposed in this work is driven by completely different forces due to contractile supracellular actomyosin bundles.

From the ALP model, we predict that the equilibrium shape of a *Hydra* fragment is determined by its anisotropy in contractility and elasticity, as shown in Fig. 2. A spherical cap shape observed in *Hydra* regeneration experiments⁷ is generated only for the case of more-or-less isotropy in both contractility (of the two contractile bundles) and elasticity (of each lamina layer). The presence of a soft mesoglea (the intermediate extracellular matrix) at given geometries (layer thicknesses) facilitates inward tissue

bending toward the endoderm side. Such proper inward bending is essential for the formation of hollow *Hydra* spheroid and the whole *Hydra* regeneration process⁷. Interestingly, the critical roles of the changes in mesoglea during *Hydra* regeneration have already been examined in experiments since the 1990s³³. However, we would like to point out that such a mesoglea-softening mechanism is very limited in ensuring inward tissue bending; we, therefore, propose to include other mechanisms, such as differential interfacial tension, as having been used to explain cell sorting during the regeneration of *Hydra* from cell aggregates³⁴.

For the bending dynamics of tissue fragments, we consider three specific dissipation mechanisms in the framework of the triple-layer ALP model: viscous drag due to the fragment motion relative to surrounding fluids, the relative frictional slide between adjacent tissue layers, and the cellular dissipation associated with sub-cellular-scale remodeling and cellular-scale rearrangements. Particularly, for rod-like fragments, we present a minimal dynamic model. The model suggests that tissue “viscosity” (specifically, the interlayer frictional sliding and cellular dissipation associated with remodeling/rearrangement at sub-cellular and cellular scales) sets the longest timescales and controls the spontaneous bending dynamics of *Hydra* fragments in the first several minutes after their excision from parent *Hydra*. In most one-layer viscoelastic models of tissue⁹ (see an example of such a model in Sec. D of Supplementary Note 2), tissue “viscosity” is simply employed as a coarse-grained concept and a “lumped” parameter to represent the underlying dissipation mechanisms. In comparison, our ALP model includes the specific tissue structure and gives predictions on the specific dissipation mechanisms. The characteristic timescale (of minutes) for the initial bending dynamics of *Hydra* fragments is obtained from parameter values measured in other independent experiments. We think this provides indirect evidence for the specific dissipation mechanisms proposed in this work. We suggest that further quantitative experiments should be done in the future to measure the elastic moduli of each tissue layer and identify the dissipation mechanisms underlying the *Hydra* regeneration process^{4–7,12}.

The proposal here on the spontaneous bending of *Hydra* tissue fragments driven by contractile supracellular actomyosin bundles should be generically present in a broad range of cell assemblies and tissue fragments during tissue regeneration or morphogenesis during embryo development^{4–6}. For example, the bending of epithelial monolayers induced by actomyosin contraction^{35,36}, out-turning of the inside of the *Volvox* embryo³⁷, etc. Our ALP model provides a useful framework for the study of tissue regeneration and morphogenesis. It connects the specific structure of the tissues with complex, emergent tissue behaviors, which is contrasted with other theoretical models for active surfaces with internal forces and torques resulting from differential stresses assumed a priori and acting along the cross-section of thin tissue sheets^{38,39}. Moreover, our ALP model can be further extended by following active gel theory^{40,41} and active nematic elastomer theory^{18,42} to be an active laminated-nematic-gel-plate (ALNGP) model to study the morphogenesis of other multi-layered tissues with supracellular nematic cytoskeletal orientation and to include the couplings between the organization of the cytoskeleton and the deformation/curvature of the tissue^{4–6}. In the ALNGP model, the topological defects can be considered by following the Landau-de Gennes theory of nematic liquid crystals⁴². The effects of the permeation of water or other small molecules on the dynamics of tissue bending can also be explored^{41,43}. Additional aspects of cell biology, such as cell division/apoptosis and cell morphological changes^{25,26}, or active behaviors such as migration and oscillations, could be incorporated as well^{24,44}. The potential of the ALP model or the extended ALNGP model can be further illustrated by numerical

simulations using the finite element method^{8,26}. For example, one can consider the spontaneous bending of circumferential *Hydra* fragments (open ring geometry)⁷ where topological defects play a role^{4–6,45}, resulting in defective morphology. One can also investigate the bending instability of tissue fragments at large deformations and study the coupling between deformation and nematic order, as well as the dynamics of topological defects during tissue morphogenesis and regeneration^{4–6}.

Methods

Active laminated-plate model (ALP) of *Hydra* tissue fragments. Here we briefly explain the ALP model of the triple-layer fragments of *Hydra* tissue. In the ALP model, the tissue fragments are treated as thin orthotropic laminated plates with internal active contraction, as shown in Fig. 1a. Following the classical laminated-plate (CLP) theory for thin orthotropic laminated plates¹⁶, the deformation of the *Hydra* tissue fragment is due entirely to the in-plane displacement $u(x, y)\hat{x}$ and $v(x, y)\hat{y}$ and the out-plane deflection (bending) $\omega(x, y)$ of the neutral surface. The components of the displacement vector are given by $u_z \approx \omega$ and

$$u_x \approx u - (z - z_{x0})\partial_x \omega, \quad u_y \approx v - (z - z_{y0})\partial_y \omega. \quad (14)$$

Note that in contrast with the traditional CLP theory, we here assume more generally that the positions of the neutral surfaces of the thin *Hydra*-laminated plate are different for the deformation in the x and y directions, and we denote them as z_{x0} and z_{y0} , respectively. Such a form of the displacement field allows the reduction of the 3D problem to one of studying the deformation of the reference neutral surfaces. Once the neutral-surface displacements (u, v, ω) are known, the displacements of any arbitrary point (x, y, z) in the 3D continuum can be determined.

Particularly, for a *Hydra*-plate suspended by its center with $\omega(0, 0) = 0$, we take the trial solution of the form

$$u = \epsilon_x x, \quad v = \epsilon_y y, \quad \omega = \frac{1}{2} (c_x x^2 + c_y y^2), \quad (15)$$

and in this case, the bending energy is given (after integrating over the thickness z -direction) by^{14,17}

$$\mathcal{F}_b = \int dx dy \left[\left(\frac{1}{2} D_{p,11} c_x^2 + D_{p,12} c_x c_y + \frac{1}{2} D_{p,22} c_y^2 \right) - \left(M_p^{(1)} c_x + M_p^{(2)} c_y \right) \right]. \quad (16)$$

Here we have used the fact that the two supracellular bundles inside *Hydra* fragments lie on the two sides of the intermediate mesoglea layer and align along the x - and y -directions in the ectoderm and endoderm layers (see Fig. 1a), respectively. $D_{p,ij}$ are the bending stiffnesses, defined by $D_{p,11} \equiv \int_{-h_1}^{h_1} dz \bar{Q}_{11} (z - z_{x0})^2$, $D_{p,12} \equiv \int_{-h_1}^{h_1} dz \bar{Q}_{12} (z - z_{x0})(z - z_{y0})$, and $D_{p,22} \equiv \int_{-h_1}^{h_1} dz \bar{Q}_{22} (z - z_{y0})^2$ with \bar{Q}_{11} , \bar{Q}_{12} , and \bar{Q}_{22} being the orthotropic elastic constants (being different in different lamina layers, see Eq. (S5) in Supplementary Information). $M_p^{(i)}$ are the active torques (per length), generated by the asymmetric internal contraction and given in the two lamina layers, respectively, by $M_p^{(1)} \approx \tau_p^{(1)} z_{x0}$ and $M_p^{(2)} \approx \tau_p^{(2)} (z_{y0} - h_m)$ with $\tau_p^{(i)} < 0$ being the active contractile forces (per length).

Onsager's principle as an approximation method for *Hydra* tissue bending dynamics.

In this work, our major purpose is not to uncover the mechanisms for the interlayer slide in *Hydra* tissue fragments, but to study the effects of interlayer slide accompanying spontaneous bending on their dynamics. Therefore, for a *Hydra* rod with differential slide and spontaneous curvature along the arc length, we neglect the in-plane contraction ϵ and simply write the total energy \mathcal{F}_t in the simple phenomenological form of Eq. (5). Minimizing \mathcal{F}_t with respect to c and ϵ_s give the spontaneous curvature and the equilibrium slide c_0 and ϵ_{s0} , respectively. Using them, the total energy in Eq. (5) can be rewritten into an alternative form as

$$\mathcal{F}_t = \int_{-\ell_c/2}^{\ell_c/2} ds \left[\frac{Y_s}{2} (\epsilon_s - \epsilon_{s0} c_0)^2 + \frac{\bar{D}_t}{2} (c - c_0)^2 \right], \quad (17)$$

with $\bar{D}_t \equiv D_t - \chi^2/Y_s$ being the normalized flexural stiffness of the rod.

To investigate the bending dynamics of *Hydra* rods, we don't study this highly nonlinear equation that has been solved numerically extensively (particularly for very long thin rods)²⁹, but instead, we carry out approximate variational analysis by assuming some trial shape dynamics of the elastic curve^{13,14}. We assume that, during the bending of the *Hydra* rod, the interlayer slide $\epsilon_s(s, t)$ and the local curvature $c(s, t)$ take some trial forms (see Fig. 3b in the main text) that are parameterized by a set of time-dependent variables $\mathbf{a}(t)$ with $-\ell_c/2 \leq s \leq \ell_c/2$ being the arc length. From the trial local curvature $c(s; \mathbf{a}(t))$, we can calculate the local tangential orientation angle $\theta(s)$ (defined relative to the horizontal x -direction) by

$$\theta(s, t) = \int_0^s c(\tilde{s}, t) d\tilde{s} + \theta(0, t), \quad (18a)$$

from which we further calculate the tangential unit vector $\hat{\mathbf{t}}(s, t)$ and position vector $\mathbf{r}(s, t)$, respectively, by

$$\hat{\mathbf{t}}(s, t) = \frac{\partial \mathbf{r}(s, t)/\partial s}{|\partial \mathbf{r}(s, t)/\partial s|} = (\cos \theta(s, t), \sin \theta(s, t)), \quad (18b)$$

$$\mathbf{r}(s, t) = \int_0^s d\tilde{s} (\cos \theta(\tilde{s}, t), \sin \theta(\tilde{s}, t)) + \mathbf{r}(0, t). \quad (18c)$$

Then using the obtained rod profile $\mathbf{r}(s, t)$, Eqs. (6) and (17), we can calculate the Rayleighian $\mathcal{R}[\dot{\mathbf{r}}, \dot{\epsilon}_s] = \dot{\mathcal{F}}_t + \Phi$ as a function of $\dot{\mathbf{a}}(t)$. Minimizing \mathcal{R} with respect to $\dot{\mathbf{a}}(t)$ gives the ordinary differential equation for $\mathbf{a}(t)$, from which we solve the bending dynamics approximately.

Bead-spring model for the bending dynamics of *Hydra* tissue fragments in viscous fluids.

In the discrete bead-spring model, we consider the dynamics of *Hydra* rods determined by the competition between the bending energy and the viscous dissipation due to the motion of the rod relative to the surrounding stationary viscous fluids. We do not consider the energy and dissipation associated with interlayer slides. Moreover, we assume the rod to be inextensible. In this case, the total energy of the *Hydra* rods includes two parts: $\mathcal{F}_t(\mathbf{r}_i(t)) = \mathcal{F}_c + \mathcal{F}_b$, which are given, respectively, by

$$\mathcal{F}_c = \sum_{i=1}^{N-1} \frac{Y_t}{2\ell_0} (r_{i,i+1} - \ell_0)^2, \quad (19)$$

$$\mathcal{F}_b = \sum_{i=1}^{N-2} \frac{D_t}{2\ell_0} [(\hat{\mathbf{t}}_{i+1} - \hat{\mathbf{t}}_i) - \phi_0 \hat{\mathbf{n}}_i]^2,$$

with $\phi_0 \equiv \ell_0 c_0 = \ell_0/R_0$ being the equilibrium bending angle. Here $r_{i,i+1} = |\mathbf{r}_{i,i+1}|$ is the distance between neighboring beads with $\mathbf{r}_{i,i+1} = \mathbf{r}_{i+1} - \mathbf{r}_i$ ($1 \leq i \leq N-1$) and $\mathbf{r}_i = (x_i, y_i)$ ($1 \leq i \leq N$) being the position vector of the i -th bead. The local tangential unit vector and normal unit vector are given, respectively, by

$$\hat{\mathbf{t}}_i \equiv \frac{\mathbf{r}_{i,i+1}}{r_{i,i+1}} = (\cos \theta_i, \sin \theta_i), \quad \hat{\mathbf{n}}_i = (-\sin \theta_i, \cos \theta_i), \quad (20)$$

in which θ_i (with $-\pi \leq \theta_i \leq \pi$) is the local tangential angle of each spring. In our simulations, we take a very large Y_t to keep the rod inextensible.

From the total energy $\mathcal{F}_t(\mathbf{r}_i(t))$ we can obtain the rate of energy change $\dot{\mathcal{F}}_t$ as a function of $\dot{\mathbf{r}}_i(t) \equiv d\mathbf{r}_i/dt$. The viscous dissipation function is given by

$$\Phi(\dot{\mathbf{r}}_i) = \sum_{i=1}^N \frac{1}{2} \xi_b \dot{\mathbf{r}}_i^2, \quad (21)$$

with $\xi_b \equiv \xi_b \ell_0$ being the effective drag coefficient of the chain segments in the surrounding viscous fluids. Then minimizing Rayleighian $\mathcal{R}(\dot{\mathbf{r}}_i) = \Phi(\dot{\mathbf{r}}_i) + \dot{\mathcal{F}}_t(\dot{\mathbf{r}}_i)$ with respect to $\dot{\mathbf{r}}_i$ gives the dynamic equations of the bead-spring chain as

$$\xi_b \frac{d\dot{\mathbf{r}}_i}{dt} = \mathbf{F}_i^s + \mathbf{F}_i^b, \quad i = 1, 2, \dots, N, \quad (22)$$

where $\mathbf{F}_i^s \equiv -\partial \mathcal{F}_c / \partial \mathbf{r}_i$ and $\mathbf{F}_i^b \equiv -\partial \mathcal{F}_b / \partial \mathbf{r}_i$ are the spring force and the bending force, respectively (see the Sec. A of Supplementary Note 2 for their expressions).

Data availability

The data that support the findings of this study are available from the authors upon request.

Code availability

The Python code for the simulations is available on the Zenodo data repository at <https://doi.org/10.5281/zenodo.8023216>⁴⁶.

Received: 2 March 2023; Accepted: 13 July 2023;

Published online: 21 July 2023

References

1. Fujisawa, T. Hydra regeneration and epitheliopeptides. *Dev. Dyn.* **226**, 182–189 (2003).
2. Takaku, Y., Hariyama, T. & Fujisawa, T. Motility of endodermal epithelial cells plays a major role in reorganizing the two epithelial layers in hydra. *Mech. Dev.* **122**, 109–122 (2005).
3. Kücken, M., Soriano, J., Pullarkat, P. A., Ott, A. & Nicola, E. M. An osmoregulatory basis for shape oscillations in regenerating hydra. *Biophys. J.* **95**, 978–985 (2008).
4. Maroudas-Sacks, Y. et al. Topological defects in the nematic order of actin fibres as organization centres of hydra morphogenesis. *Nat. Phys.* **17**, 251–259 (2021).

5. Maroudas-Sacks, Y. & Keren, K. Mechanical patterning in animal morphogenesis. *Annu. Rev. Cell Dev. Biol.* **37**, 469–493 (2021).
6. Maroudas-Sacks, Y. & Keren, K. Supra-cellular actin fiber arrays and their role in animal morphogenesis. *Phys. Biol.* **18**, 041501–14 (2021).
7. Livshits, A., Shani-Zerbib, L., Maroudas-Sacks, Y., Braun, E. & Keren, K. Structural inheritance of the actin cytoskeletal organization determines the body axis in regenerating hydra. *Cell Rep.* **18**, 1410–1421 (2017).
8. Krahe, M. et al. Fluctuations and differential contraction during regeneration of hydra vulgaris tissue toroids. *New J. Phys.* **15**, 035004 (2013).
9. Carter, J. A., Hyland, C., Steele, R. E. & Collins, E.-M. S. Dynamics of mouth opening in hydra. *Biophys. J.* **110**, 1191–1201 (2016).
10. Lou, Y. et al. Interfacial friction and substrate deformation mediate long-range signal propagation in tissues. *Biomech. Model. Mechanobiol.* **21**, 1511–1530 (2022).
11. Guevorkian, K., Colbert, M.-J., Durth, M., Dufour, S. & Brochard-Wyart, F. Aspiration of biological viscoelastic drops. *Phys. Rev. Lett.* **104**, 218101 (2010).
12. Rieu, J. P., Upadhyaya, A., Glazier, J. A., Ouchi, N. B. & Sawada, Y. Diffusion and deformations of single hydra cells in cellular aggregates. *Biophys. J.* **79**, 1903–1914 (2000).
13. Doi, M. Onsager principle in polymer dynamics. *Prog. Polym. Sci.* **112**, 101339 (2021).
14. Wang, H., Qian, T. & Xu, X. Onsager’s variational principle in active soft matter. *Soft Matter* **17**, 3634–3653 (2021).
15. Landau, L. D. & Lifshitz, E. M. *Theory of Elasticity*, Vol. 7 of *Course of Theoretical Physics* 3rd edn (Pergamon Press, 1986).
16. Reddy, J. N. *Mechanics of Laminated Composite Plates and Shells: Theory and Analysis* (CRC Press, 2003).
17. Wang, H., Zou, B., Su, J., Wang, D. & Xu, X. Variational methods and deep ritz method for active elastic solids. *Soft Matter* **18**, 6015–6031 (2022).
18. Warner, M., Modes, C. D. & Corbett, D. Curvature in nematic elastica responding to light and heat. *Proc. Math. Phys. Eng. Sci.* **466**, 2975–2989 (2010).
19. Van Rees, W. M., Vouga, E. & Mahadevan, L. Growth patterns for shape-shifting elastic bilayers. *Proc. Natl Acad. Sci. USA* **114**, 11597–11602 (2017).
20. Armon, S., Efrati, E., Kupferman, R. & Sharon, E. Geometry and mechanics in the opening of chiral seed pods. *Science* **333**, 1726–1730 (2011).
21. Biton, Y. & Safran, S. The cellular response to curvature-induced stress. *Phys. Biol.* **6**, 046010 (2009).
22. Friedrich, B. M. & Safran, S. A. How cells feel their substrate: spontaneous symmetry breaking of active surface stresses. *Soft Matter* **8**, 3223–3230 (2012).
23. Callens, S. J., Uyttendaele, R. J., Fratila-Apachitei, L. E. & Zadpoor, A. A. Substrate curvature as a cue to guide spatiotemporal cell and tissue organization. *Biomaterials* **232**, 119739 (2020).
24. Šiber, A. & Zihnerl, P. *Cellular Patterns* (CRC Press, 2017).
25. Hannezo, E., Prost, J. & Joanny, J.-F. Theory of epithelial sheet morphology in three dimensions. *Proc. Natl Acad. Sci. USA* **111**, 27–32 (2014).
26. Ackermann, J., Qu, P.-Q., LeGoff, L. & Ben Amar, M. Modeling the mechanics of growing epithelia with a bilayer plate theory. *Eur. Phys. J. Plus* **137**, 1–29 (2022).
27. Srolovitz, D., Safran, S. & Tenne, R. Elastic equilibrium of curved thin films. *Phys. Rev. E* **49**, 5260 (1994).
28. Tadrif, L., Brochard-Wyart, F. & Couvélér, D. Bilayer curling and winding in a viscous fluid. *Soft Matter* **8**, 8517–8522 (2012).
29. Callan-Jones, A., Brun, P.-T. & Audoly, B. Self-similar curling of a naturally curved elastica. *Phys. Rev. Lett.* **108**, 174302 (2012).
30. Safran, S. A. *Statistical Thermodynamics of Surfaces, Interfaces, and Membranes* (CRC Press, 2018).
31. Schötz, E.-M. et al. Quantitative differences in tissue surface tension influence zebrafish germ layer positioning. *HFSP J.* **2**, 42–56 (2008).
32. Timoshenko, S. Analysis of bi-metal thermostats. *J. Opt. Soc. Am.* **11**, 233–255 (1925).
33. Sarras Jr, M. P. et al. Extracellular matrix (mesoglea) of hydra vulgaris: Iii. formation and function during morphogenesis of hydra cell aggregates. *Dev. Biol.* **157**, 383–398 (1993).
34. Briscoe, J. & Kicheva, A. The physics of development 100 years after d’arcy thompson’s “on growth and form”. *Mech. Dev.* **145**, 26–31 (2017).
35. Morris, R. G. & Rao, M. Active morphogenesis of epithelial monolayers. *Phys. Rev. E* **100**, 022413 (2019).
36. Fouchard, J. et al. Curling of epithelial monolayers reveals coupling between active bending and tissue tension. *Proc. Natl Acad. Sci. USA* **117**, 9377–9383 (2020).
37. Höhn, S., Honerkamp-Smith, A. R., Haas, P. A., Trong, P. K. & Goldstein, R. E. Dynamics of a Volvox embryo turning itself inside out. *Phys. Rev. Lett.* **114**, 1–5 (2015).
38. Salbreux, G. & Jülicher, F. Mechanics of active surfaces. *Phys. Rev. E* **96**, 1–20 (2017).
39. Khoromskaia, D. & Salbreux, G. Active morphogenesis of patterned epithelial shells. *eLife* **12**, e75878 (2023).
40. Prost, J., Jülicher, F. & Joanny, J.-F. Active gel physics. *Nat. Phys.* **11**, 111–117 (2015).
41. Callan-Jones, A. C. & Jülicher, F. Hydrodynamics of active permeating gels. *New J. Phys.* **13**, 093027 (2011).
42. He, S. et al. A theoretical model of collective cell polarization and alignment. *J. Mech. Phys. Solids* **137**, 103860 (2020).
43. Ding, Z., Lyu, P., Shi, A., Man, X. & Doi, M. Diffusio-mechanical theory of gel bending induced by liquid penetration. *Macromolecules* **55**, 7092–7099 (2022).
44. Popović, M. et al. Active dynamics of tissue shear flow. *New J. Phys.* **19**, 033006 (2017).
45. Pearce, D., Gat, S., Livne, G., Bernheim-Groswasser, A. & Kruse, K. Defect-driven shape transitions in elastic active nematic shells. Preprint at arXiv:2010.13141 (2020).
46. Su, J., Wang, H., Yan, Z. & Xu, X. Code for “active laminated-plate model for spontaneous bending of Hydra tissue fragments driven by supracellular actomyosin bundles”. *Zenodo* (2023).

Acknowledgements

The authors thank Samuel Safran, Kinneret Keren, Zhihao Li, Yonit Maroudas-Sacks, Lital Shani-Zerbib, and Anton Livshits for fruitful discussions. X.X. is supported in part by the National Natural Science Foundation of China (NSFC, No. 12004082) and by the 2020 Li Ka Shing Foundation Cross-Disciplinary Research Grant (No. 2020LKSF08A). The simulations in this work were carried out at the Shanxi Supercomputing Center of China, and the calculations were performed on TianHe-2.

Author contributions

X.X. conceived the research. J.S., H.W., and X.X. developed the theory. J.S. and Z.Y. designed and carried out the simulations. All authors analyzed the data and wrote the paper. J.S. and H.W. contributed equally to this work.

Competing interests

The authors declare no competing interests.

Additional information

Supplementary information The online version contains supplementary material available at <https://doi.org/10.1038/s42005-023-01307-9>.

Correspondence and requests for materials should be addressed to Xinpeng Xu.

Peer review information *Communications Physics* thanks the anonymous reviewers for their contribution to the peer review of this work. A peer review file is available.

Reprints and permission information is available at <http://www.nature.com/reprints>

Publisher’s note Springer Nature remains neutral with regard to jurisdictional claims in published maps and institutional affiliations.



Open Access This article is licensed under a Creative Commons Attribution 4.0 International License, which permits use, sharing, adaptation, distribution and reproduction in any medium or format, as long as you give appropriate credit to the original author(s) and the source, provide a link to the Creative Commons license, and indicate if changes were made. The images or other third party material in this article are included in the article’s Creative Commons license, unless indicated otherwise in a credit line to the material. If material is not included in the article’s Creative Commons license and your intended use is not permitted by statutory regulation or exceeds the permitted use, you will need to obtain permission directly from the copyright holder. To view a copy of this license, visit <http://creativecommons.org/licenses/by/4.0/>.

© The Author(s) 2023